Automatic Take-Off of a Tethered Aircraft for Airborne Wind Energy: Control Design and Experimental Results

L. Fagiano * **E. Nguyen-Van** ** **F. Rager** ** **S. Schnez** ** **C. Ohler** **

* *Politecnico di Milano, Dipartimento di Elettronica, Informazione e Bioingegneria, Milano, Italy (e-mail: lorenzo.fagiano@polimi.it)*
** *ABB Switzerland, Corporate Research, Baden-Dättwil, Switzerland. (e-mail: eric.nguyenvan@protonmail.ch, {felix.rager | stephan.schnez | christian.ohler}@ch.abb.com)*

Abstract: A control approach to realize the autonomous take-off of a tethered aircraft is described, and experimental results on a small-scale prototype are presented. The plant comprises a ground station, equipped with a linear motion system and a controlled winch, connected to a tethered rigid aircraft. The linear motion system is used to accelerate the aircraft to take-off speed. The winch controller has to coordinate the tether reeling with the aircraft motion, to avoid stalling the aircraft while at the same time preventing tether entanglement, and the aircraft controller has to stabilize the attitude and carry out a straight-line climbing phase, followed by repetitive figure-of-eight patterns at constant altitude. The proposed control approach is fully decoupled, i.e. there is no exchange of information between the ground station and the aircraft. The experimental tests show that the designed control system is able to achieve successful and repeatable take-off maneuvers in very compact space. This result is relevant for the ongoing development of airborne wind energy systems, which exploit the flight of tethered aircrafts to convert wind energy into electricity.

Keywords: Airborne Wind Energy, High-Altitude Wind Energy, Wind Energy, Tethered Aircraft, Autonomous Flight, Autonomous Take-Off, Unmanned Aerial Vehicle.

1. INTRODUCTION

Airborne Wind Energy (AWE) technologies aim to convert wind energy into electricity by using tethered aircrafts, see e.g. the book edited by Ahrens et al. (2013). First envisioned in the late '70s (Loyd (1980)), AWE concepts have been significantly developed in the last decade, with the growth of a community of research groups and companies worldwide and the realization of small-scale prototypes exploring different possible variants of the same basic idea. Today, a number of AWE technologies employ an electric generator installed on ground, linked to a winch where the tether is coiled, and they generate electricity by repeatedly reeling-out and -in the tether, see e.g. Ruiterkamp and Sieberling (2013); Bormann et al. (2013); van der Vlugt et al. (2013); Erhard and Strauch (2015). Notwithstanding the significant achievements and continuous improvements made in the last years, with contributions mainly concerned with aerodynamics and controls (see e.g. Breukels et al. (2014); Zgraggen et al. (2016); Erhard and Strauch (2015)), one problem that is still open for these systems is the aircraft's capability to take-off autonomously in compact space without large extra-costs, e.g. due to additional required equipments. Focusing on systems with rigid aircrafts, there is in fact evidence of autonomous take-off (Ruiterkamp and Sieberling (2013)), however with a winch launch that requires a significant space in all directions in order to adapt to different wind conditions. In the scientific literature, Gros et al. (2013) presented a simulation study for a rotational take-off, while Bontekoe (2010) carried out an analysis of several approaches, deeming three alternatives as the most promising ones: buoyant systems, linear ground acceleration plus on-board propeller, and rotational take-off. Then, the rotational take-off is examined in more detail by means of numerical simulations. Fagiano and Schnez (2015) presented a theoretical analysis, which shows how a linear take-off approach appears to be the most viable one, according to different performance criteria.

In a recent research activity carried out at ABB Corporate Research, we delivered a small-scale experimental demonstration of a linear take-off approach, starting from the theoretical results of Fagiano and Schnez (2015). The experimental results show that a fully autonomous take-off can be realized in very compact space, with a rather small additional power on the ground station to accelerate the aircraft. In this paper, we provide an overview of the control strategy and design approach, and we present the experimental results. To the best of our knowledge, this is the first experimental demonstration of this approach that is divulged in the scientific literature. Due to space limitations, we cannot describe here the full details of the prototype design, neither of the modeling, identification and control design phases. For such additional details, we refer the interested reader to two contributions in an open repository, see Fagiano et al. (2016c) and Fagiano et al. (2016a). A movie of the tests is also available on-line, see Fagiano et al. (2016b).

2. PROTOTYPE LAYOUT AND OPERATION

A rendering of our small-scale prototype is shown in Fig. 1, highlighting all the main mechanical components. The system is composed of two main subsystems, the ground

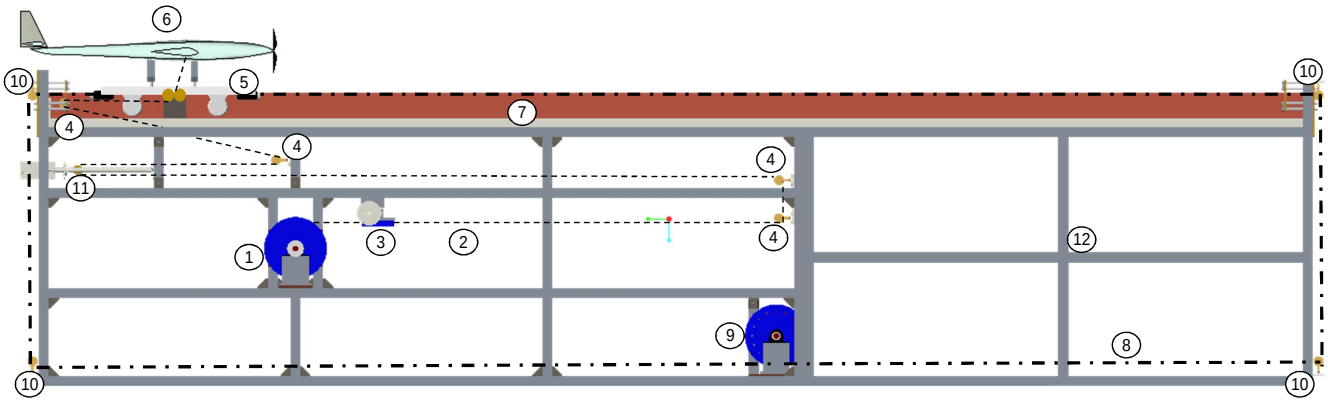

Fig. 1. Rendering of the small-scale prototype built at ABB Corporate Research. The numbers in the picture indicate: 1. the winch, 2. the tether connected to the aircraft (dashed line), 3. the spooling mechanism, 4. the series of pulleys that redirect the tether from the winch to the aircraft, 5. the slide, 6. the aircraft, 7. the rails, 8. the tether used to pull the slide in backward/forward directions ("slide tether", dash-dotted line), 9. the drum hosting the slide tether, 10. the pulleys that redirect the slide tether, 11. the mass-spring system, 12. the frame. As a reference, the rails' length in this rendering is 5.2 m.

station and the aircraft, connected by a tether. The latter is coiled around a winch and passes through a series of pulleys before attaching to the aircraft. One of the pulleys which the tether passes through is installed on a moving plate, connected to a spring whose compression is measured by a potentiometer. This subsystem is used to reduce the stiffness of the link between the ground station and the aircraft and to control the winch speed, as described in Section 3.1.

Before take-off, the aircraft is installed on a slide, able to move on rails and controlled by a linear motion system, which in our prototype is composed of a second tether wound around a drum ("slide drum") and connected to both ends of the slide via another series of pulleys. The winch and the slide drum are each connected to an electric motor, controlled by a drive. The ground station controller acquires the motors' position measurements from the drives and the spring's compression from the potentiometer, and computes the reference position and speed values for the slide and winch motors, respectively, which are then sent back to the drives. Regarding the aircraft, its main components are a tether attachment and release mechanism, a front propeller, the typical control surfaces (ailerons, elevator, rudder and flaps), an onboard electronic control unit, a radio receiver linked to a remote controller, employed by a pilot on ground, finally onboard position, inertial, attitude and airspeed sensors.

The operation of the described system is the following: when the take-off procedure starts, the ground station control system accelerates the aircraft up to take-off speed, using about half of the rails' length (the second half being needed to brake the slide). At the same time, the winch has to accelerate in a synchronized way with the slide, in order to reel-out the tether at just the right speed to avoid pulling on the aircraft (which would quickly cause a stall condition) while also avoiding to entangle the tether due to an excessive reel-out with no pulling force. This is achieved by a feedforward/feedback control strategy described in Section 3.1. The aircraft has to coordinate with the ground station to ramp up the propeller and carry out a quick climb to a safe altitude, followed by repetitive figure-of-eight flight paths above the ground station, at roughly constant altitude. In the latter phase, the winch controller has to still regulate the reeling speed to fulfill the same conflicting objectives (low pulling force and low tether sag/no entanglement) while the aircraft periodically approaches and veers-off from the ground station.

3. CONTROL DESIGN

In this application, the most critical problem to be solved is the coordination between the ground station and the aircraft. In our approach, we adopt a completely decoupled strategy to address this aspect, where the controller of the ground station and the one on the aircraft do not exchange any information. Rather, the ground station controller exploits the local measurement of the spring compression to adjust the reeling speed, while the onboard controller deals with the resulting tether force as an external disturbance. We therefore present the two local controllers as fully separated entities, each one with its own control objectives and design approach.

3.1 Ground station control

We adopt a hierarchical control structure: inner feedback control loops programmed on the drives track references of position (for the slide) and speed (for the winch), which are computed by an outer control loop programmed on the ground station central controller. All control loops are implemented in discrete time with sampling period T_s; we denote with $k \in \mathbb{Z}$ the discrete time instants.

For the inner loops we employ static state-feedback controllers designed via pole-placement, using a standard linear model of the motors which takes into account their inertia and viscous friction. Since these parameters can be identified precisely and the state (position and speed) of each motor is accurately measured by the drives, the resulting controllers feature very high performance and robustness. Denoting with the subscript "$_\mathrm{s}$" and "$_\mathrm{w}$" quantities related to the slide and the winch motors, respectively, the control laws for the inner loops are:

$$u_\mathrm{s}(k) = K_{\theta,\mathrm{s}}(\theta_{\mathrm{ref,s}}(k) - \theta_\mathrm{s}(k)) - K_{\dot\theta,\mathrm{s}}\,\dot\theta_\mathrm{s}(k) \tag{1a}$$

$$u_\mathrm{w}(k) = K_{\dot\theta,\mathrm{w}}(\dot\theta_{\mathrm{ref,w}}(k) - \dot\theta_\mathrm{w}(k)) \tag{1b}$$

where u_s, u_w are the commanded torques, θ_s, θ_w the angular positions of the motors, $\theta_{\mathrm{ref,s}}$ the reference position for the slide motor, $\dot\theta_{\mathrm{ref,w}}$ the reference speed for the winch

motor, and $K_{\theta,\mathrm{s}}$, $K_{\dot{\theta},\mathrm{s}}$, $K_{\dot{\theta},\mathrm{w}}$ the feedback gains.

Regarding the outer control loops, we assume that the slide is initially positioned at one end of the rails. Without loss of generality, let us assume that $k = 0$ when the take-off maneuver starts. Then, the outer controller for the slide motor issues a step of position reference $\theta_{\mathrm{ref,s}}(k) = L/R_{\mathrm{s}}, \forall k > 0$, where L is the desired slide travel used for take-off and R_{s} the radius of the slide drum. As a consequence, the inner controller for the slide moves it quickly to the new reference position and, during this motion, the take-off speed of the aircraft is reached. At the same time, the winch has to coordinate with the slide and achieve at all times a good trade-off between limiting the pulling force exerted by the tether and avoiding tether entanglement. To achieve this goal throughout the take-off and flight, we employ a combined feedforward/feedback approach to compute the reference winch speed. The feedforward contribution latches the winch speed to the slide speed:

$$\dot{\theta}^{\mathrm{ffwd}}_{\mathrm{ref,w}}(k) = \gamma \dot{\theta}_{\mathrm{s}}(k) \tag{2}$$

where $\gamma \approx 1$ is a scalar that can be tuned to achieve a good coordination between the two drums. The feedback contribution exploits the measure of the spring travel, denoted with $x_{\mathrm{s}}(k)$. In particular, we set two threshold values, x^I_{s}, x^{II}_{s}, which divide the available spring travel in three zones:

- **Zone a** ($0 \leq x_{\mathrm{s}}(k) \leq x^I_{\mathrm{s}}$): the spring is practically uncompressed (low tether force), the winch shall decrease speed and eventually reel-in;
- **Zone b** ($x^I_{\mathrm{s}} < x_{\mathrm{s}}(k) < x^{II}_{\mathrm{s}}$): the spring is subject to low force, the winch shall be held in place (constant tether length);
- **Zone c**: ($x^{II}_{\mathrm{s}} \leq x_{\mathrm{s}}(k) \leq \overline{x}_{\mathrm{s}}$): the spring is subject to relatively large force, the winch shall increase its speed and reel-out to release the tether.

Then, the feedback contribution to the reference winch speed is computed according to the following strategy (see Fig. 2):

$$\begin{aligned}
&\texttt{If } 0 \leq x_{\mathrm{s}}(k) < x^I_{\mathrm{s}} \text{ (\textbf{Zone a})} \\
&\quad \bar{x}_{\mathrm{s}}(k) = \frac{x_{\mathrm{s}}(k) - x^I_{\mathrm{s}}}{x^{I,\mathrm{a}}_{\mathrm{s}} - x^I_{\mathrm{s}}} \\
&\quad \dot{\theta}^{\mathrm{fbck}}_{\mathrm{ref,w}}(k) = \min\left(0, \max\left(\underline{\dot{\theta}}^{\mathrm{fbck}}_{\mathrm{ref,w}}, \left(\dot{\theta}^{\mathrm{fbck}}_{\mathrm{ref,w}}(k-1) + T_s \ddot{\theta}^{\mathrm{a}}_{\mathrm{ref,w}} \bar{x}_{\mathrm{s}}(k)\right)\right)\right) \\
&\texttt{Else if } x^I_{\mathrm{s}} \leq x_{\mathrm{s}}(k) < x^{II}_{\mathrm{s}} \text{ (\textbf{Zone b})} \\
&\quad \dot{\theta}^{\mathrm{fbck}}_{\mathrm{ref,w}}(k) = \dot{\theta}^{\mathrm{fbck}}_{\mathrm{ref,w}}(k-1) \\
&\texttt{Else if } x^{II}_{\mathrm{s}} \leq x_{\mathrm{s}}(k) \leq \overline{x}_{\mathrm{s}} \text{ (\textbf{Zone c})} \\
&\quad \bar{x}_{\mathrm{s}}(k) = \frac{x_{\mathrm{s}}(k) - x^{II}_{\mathrm{s}}}{x^{II,\mathrm{c}}_{\mathrm{s}} - x^{II}_{\mathrm{s}}} \\
&\quad \dot{\theta}^{\mathrm{fbck}}_{\mathrm{ref,w}}(k) = \max\left(0, \min\left(\overline{\dot{\theta}}^{\mathrm{fbck}}_{\mathrm{ref,w}}, \left(\dot{\theta}^{\mathrm{fbck}}_{\mathrm{ref,w}}(k-1) + T_s \ddot{\theta}^{\mathrm{c}}_{\mathrm{ref,w}} \bar{x}_{\mathrm{s}}(k)\right)\right)\right)
\end{aligned} \tag{3}$$

where $\underline{\dot{\theta}}^{\mathrm{fbck}}_{\mathrm{ref,w}}$, $\overline{\dot{\theta}}^{\mathrm{fbck}}_{\mathrm{ref,w}}$ are the desired minimum and maximum reference speed values that can be issued, and $\ddot{\theta}^{\mathrm{a}}_{\mathrm{ref,w}}$, $\ddot{\theta}^{\mathrm{c}}_{\mathrm{ref,w}}$ are the desired angular accelerations for the reference speed. Such values are scaled according to the position of the potentiometer relative to the fixed positions (design parameters) $x^{I,\mathrm{a}}_{\mathrm{s}} < x^I_{\mathrm{s}}$ and $x^{II,\mathrm{c}}_{\mathrm{s}} > x^{II}_{\mathrm{s}}$, respectively for zones **a** and **c**. Equation (3) represents an integral controller, where the integrated quantity is the distance of the spring position $x_{\mathrm{s}}(k)$ from the interval $(x^I_{\mathrm{s}}, x^{II}_{\mathrm{s}})$ (i.e. zone **b**) and the gain is piecewise constant, since it is different in zones **a** and **c**. Moreover, a saturation of the integrated variable to negative (resp. positive) values is operated whenever the spring enters zone **a** (resp. **c**), in order to quickly start to reel-in (resp. reel-out) when the tether is released (resp. pulled). A sensible choice for the involved design parameters is $\underline{\dot{\theta}}^{\mathrm{fbck}}_{\mathrm{ref,w}}$, $\ddot{\theta}^{\mathrm{a}}_{\mathrm{ref,w}} < 0$, $\overline{\dot{\theta}}^{\mathrm{fbck}}_{\mathrm{ref,w}}$, $\ddot{\theta}^{\mathrm{c}}_{\mathrm{ref,w}} > 0$, $x^{I,c}_{\mathrm{s}} \approx x^I_{\mathrm{s}}/2$ and $x^{I,c}_{\mathrm{s}} \approx (\overline{x}_{\mathrm{s}} + x^{II}_{\mathrm{s}})/2$.

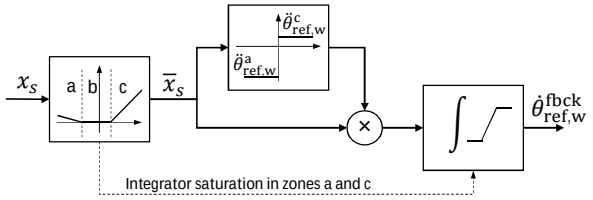

Fig. 2. Block-diagram of the feedback contribution to the reference winch speed.

Finally, the reference speed issued to the low-level controller is computed as:

$$\begin{aligned}
&\texttt{If } \dot{\theta}_{\mathrm{s}}(k) > 0 \\
&\quad \dot{\theta}_{\mathrm{ref,w}}(k) = \max\left(\dot{\theta}^{\mathrm{ffwd}}_{\mathrm{ref,w}}(k), \dot{\theta}^{\mathrm{fbck}}_{\mathrm{ref,w}}(k)\right) \\
&\texttt{Else} \\
&\quad \dot{\theta}_{\mathrm{ref,w}}(k) = \dot{\theta}^{\mathrm{fbck}}_{\mathrm{ref,w}}(k)
\end{aligned} \tag{4}$$

According to (4), the feedforward contribution is used only if larger than the feedback one, and only if the speed of the slide is positive, i.e. during take-off.

3.2 Aircraft control

Control objectives and aircraft model. We divide the operation of the onboard controller in two subsequent phases, whose control objectives are described next.

Take-Off and climbing: The onboard controller has to detect the take-off situation and stabilize the aircraft's attitude while at the same time powering up the onboard motor to sustain the climb and reach a safe altitude, before performing any other maneuver.

Transition phase and figure-of-eight patterns: Once a safe altitude has been reached, the controller shall carry out a transition maneuver to engage a repetitive figure-of-eight pattern parallel to the ground at a target altitude.

We propose a model-based control design approach, where we adopt a very simple model of the aircraft dynamics, with the same spirit of previous contributions on AWE control design, see e.g. Erhard and Strauch (2012); Fagiano et al. (2014); Erhard and Strauch (2015). We start by introducing an inertial coordinate system (X, Y, Z) fixed to the ground, and a local one (x, y, z) fixed to the aircraft (body frame). The position vector of the aircraft is denoted by $\boldsymbol{p}$, its velocity by $\dot{\boldsymbol{p}} \doteq d\boldsymbol{p}/dt$, where t is the continuous time variable. When considering the components of a vector, we add as a subscript the corresponding axis, e.g. p_X is the component of vector $\boldsymbol{p}$ along the inertial $X-$axis. We further denote by φ, θ, ψ the standard roll, pitch and yaw angles (Euler angles), and with v_a the magnitude of the airspeed along the body $x-$axis direction. The value of v_a is measured thanks to the onboard pitot probe aligned

with the body $x-$axis. Finally, we denote with u_φ, u_θ and u_m the control inputs for the ailerons, elevator, and propeller thrust, respectively.

The first set of model equations describe the turning behavior of the aircraft, starting from the roll angle dynamics:

$$\ddot{\varphi}(t) = a_\varphi \dot{\varphi}(t) + b_\varphi u_\varphi(t) + d_\varphi(t) \tag{5}$$

where a_φ and b_φ are parameters to be identified, and d_φ is a disturbance term accounting for neglected dynamics, wind, and the presence of the tether. Details on the assumptions underlying this model and on the parameter identification approach can be found in Fagiano et al. (2016a), where a very good matching between the model and experimental data is shown.
Considering a turning maneuver at constant tangential speed and with constant radius along a circular trajectory roughly parallel to the ground, the roll angle φ can be then linked to the lateral acceleration of the aircraft by the equilibrium of aerodynamic lift, gravitational force, and centrifugal force during the turn:

$$L\sin(\varphi) = m a_y \tag{6a}$$

$$L\cos(\varphi) = mg \tag{6b}$$

where L is the aerodynamic lift force, m the mass of the aircraft, and a_y is the centripetal acceleration. As mentioned, such equations hold with good approximation when the path is parallel to the ground, such that when $\varphi = 0$ the lift force points along the inertial Z direction. Moreover, under the considered assumptions, the tangential speed equals $|\dot{\boldsymbol{p}}(t)|$ and from the kinematics of rigid bodies we have:

$$a_y = |\dot{\boldsymbol{p}}(t)|\dot{\psi} \tag{7}$$

where $\dot{\psi}$ is the yaw rate. Now, inserting (7) into (6a), dividing (6a) by (6b) and assuming small roll angles, we obtain:

$$\dot{\psi}(t) = \frac{g}{|\dot{\boldsymbol{p}}(t)|}\varphi(t) \tag{8}$$

Finally, it is useful to also introduce the link between the trajectory curvature $1/R(t)$ (where $R(t)$ is the turning radius) and the roll angle. Considering that $\dot{\psi}(t) \simeq \dfrac{|\dot{\boldsymbol{p}}(t)|}{R(t)}$, we have:

$$\frac{1}{R(t)} = \frac{g}{|\dot{\boldsymbol{p}}(t)|^2}\varphi(t) \tag{9}$$

Together, equations (5) and (8)-(9) form our model for the turning behavior, since they link the aileron input to the roll angle, and the latter to the flown trajectory on a plane parallel to the ground.
As regards the vertical motion, we start from the pitch dynamics:

$$\ddot{\theta}(t) = a_\theta \dot{\theta}(t) + b_\theta u_\theta(t) + d_\theta(t) \tag{10}$$

where, in a way similar to equation (5), a_θ and b_θ are unknown parameters to be identified and d_θ accounts for neglected effects. Assuming now a straight-line flight parallel to the ground at constant forward speed, a constant pitch value θ_0 exists, such that this motion is at steady state, i.e. the lift force equals the weight of the aircraft and the propeller's thrust counteracts the drag. For simplicity and without loss of generality, we assume $\theta_0 = 0$. Exploiting again the assumption of small θ values, we can then approximate the link between the pitch angle and the vertical velocity along the inertial $Z-$axis as:

$$\dot{p}_Z(t) = |\dot{\boldsymbol{p}}(t)|\theta(t) \tag{11}$$

Fig. 3 provides a graphical interpretation of (11). Equations (10) and (11) link the pitch dynamics to the vertical inertial component of the aircraft trajectory, and form our

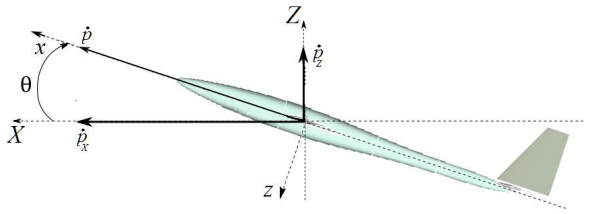

Fig. 3. Sketch of the considered pitch/vertical motion model for the aircraft

model of the vertical dynamics. Also in this case there are only few parameters, which can be easily identified from experimental data.
Last, we employ the following equations to model the effect of the propeller thrust on the airspeed v_a:

$$u_\mathrm{m}(t) = \frac{1}{2}\rho A C_D v_a(t)^2 + d_{v_a}(t) \tag{12}$$

where ρ is the air density, C_D the aerodynamic drag coefficient, A the effective area of the aircraft, and $d_{v_a}(t)$ a term accounting for neglected effects. Equation (12) is derived by assuming equilibrium between the motor thrust and the aerodynamic drag, and a small angle of attack.

Equations (5) and (8)-(12) form the model of the aircraft that we will use for control design. The only unknown parameters are a_φ, b_φ, a_θ, b_θ, which can be identified from data as shown in Fagiano et al. (2016a).

Control design. We employ a hierarchical control structure (see Fig. 4), with low-level controllers designed to track reference values for the roll angle, φ_ref, pitch angle, θ_ref, and front airspeed, $v_{a,\mathrm{ref}}$, and high-level controllers that compute such references in order to achieve the goals described above for each operational phase. The employed

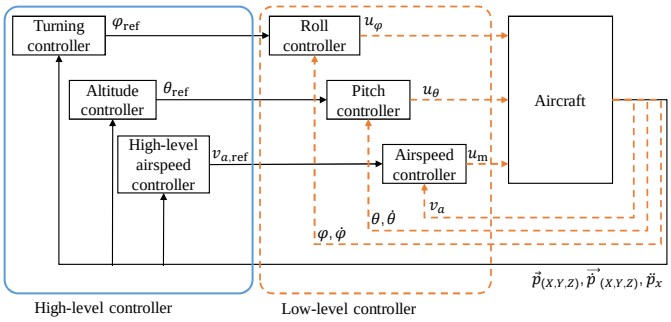

Fig. 4. Controller architecture showing the feedback variables used by the three low-level controllers and by the corresponding three high-level controllers.

control inputs are the aileron and elevator positions, u_φ and u_θ, and the propeller thrust, u_m.

Regarding the inner control loops, since φ, $\dot{\varphi}$, θ, $\dot{\theta}$, and v_a are directly measured and their dynamics are approximately linear for the sake of our goals (see (5) and (10)), we use static, linear state-feedback control laws to stabilize these quantities and track their reference values. For the roll dynamics, we define the angular tracking error as

$$e_\varphi(t) \doteq \varphi_\mathrm{ref}(t) - \varphi(t), \tag{13}$$

and employ the state-feedback control law

$$u_\varphi(t) = K_{e_\varphi}\, e_\varphi(t) + K_{\dot{e}_\varphi}\dot{e}_\varphi(t). \tag{14}$$

From (5) and (13)-(14) we have:

$$\begin{bmatrix} \dot{e}_\varphi(t) \\ \ddot{e}_\varphi(t) \end{bmatrix} = \underbrace{\begin{bmatrix} 0 & 1 \\ -b_\varphi K_{e_\varphi} & a_\varphi - b_\varphi K_{\dot{e}_\varphi} \end{bmatrix}}_{A_{\varphi,CL}} \begin{bmatrix} e_\varphi(t) \\ \dot{e}_\varphi(t) \end{bmatrix} + \begin{bmatrix} 0 \\ w_\varphi(t) \end{bmatrix} \tag{15}$$

where $w_\varphi(t) \doteq (\ddot{\varphi}_{\text{ref}}(t) - d_\varphi(t) - a_\varphi \dot{\varphi}_{\text{ref}})$ can be seen as an external, bounded disturbance term accounting for neglected dynamics and the time variation of the reference roll angle and rate issued by the high-level controller. We use a classical pole-placement technique (Goodwin et al. (2001)) to design the gains K_{e_φ}, $K_{\dot{e}_\varphi}$ in order to assign the eigenvalues $\lambda_{\varphi,1}$, $\lambda_{\varphi,2}$ (design parameters) of the matrix $A_{\varphi,CL}$ describing the closed-loop dynamics of the tracking error.

Following the same approach, we design the low-level controller for the pitch as:

$$e_\theta(t) \doteq \theta_{\text{ref}}(t) - \theta(t) \tag{16a}$$

$$u_\theta(t) = K_{e_\theta}\, e_\theta(t) + K_{\dot{e}_\theta} \dot{e}_\theta(t) \tag{16b}$$

where the gains K_{e_θ}, $K_{\dot{e}_\theta}$ are computed to assign the closed-loop poles $\lambda_{\vartheta,1}$, $\lambda_{\vartheta,2}$. Finally, for the airspeed controller we employ a static law as well, however considering the square of the airspeed and of its reference:

$$u_{\text{m}}(t) = K_{\text{m}} \left(v_{a,\text{ref}}^2(t) - v_a^2(t) \right), \tag{17}$$

where $K_{\text{m}} > 0$ is a design parameter. From (12) and (17) we obtain the closed-loop relationship:

$$v_a(t) = \sqrt{\frac{K_{\text{m}}}{K_{\text{m}} + \frac{1}{2}\rho A C_D} v_{a,\text{ref}}^2(t) + \frac{1}{K_{\text{m}} + \frac{1}{2}\rho A C_D} d_{v_a}(t)} \tag{18}$$

which for large enough values of K_{m} (as compared with the terms $\frac{1}{2}\rho A C_D$ and $d_{v_a}(t)$) gives:

$$v_a(t) \approx v_{a,\text{ref}}(t).$$

While the low-level controllers never change during operation, we design different high-level control strategies according to the operational phases outlined above, and we switch among them when a transition from the first phase to the second one is detected.

Take-Off and climbing. In this phase, the aircraft is initially at rest on the slide, waiting for the acceleration provided by the latter. A minimum forward acceleration threshold $\underline{\ddot{p}}_{x,\text{to}}$ is set by the control designer to detect the start of the take-off. When the following condition is detected:

$$\ddot{p}_x \geq \underline{\ddot{p}}_{x,\text{to}} \tag{19}$$

then a constant airspeed reference is issued:

$$v_{a,\text{ref}}(t) = v_{a,\text{ref,to}}, \tag{20}$$

where the design parameter $v_{a,\text{ref,to}}$ is chosen as a much larger value than the cruise airspeed of the aircraft, in order to provide full propeller thrust during the initial climb. Regarding the altitude controller, a constant, relatively large reference pitch angle (e.g. 40°) is used:

$$\theta_{\text{ref}}(t) = \theta_{\text{ref,to}} \tag{21}$$

which gives place to a large vertical speed (see equation (11)). Finally, the roll reference is computed in order to keep a straight trajectory in the inertial (X, Y) plane. To this end, we consider the course angle:

$$\gamma(t) = \arctan\left(\frac{\dot{p}_Y(t)}{\dot{p}_X(t)} \right) \tag{22}$$

and we employ the following feedback controller:

$$\varphi_{\text{ref}}(t) = K_\varphi \frac{|\dot{\boldsymbol{p}}(t)|}{g} \left(\gamma_{\text{ref,to}} - \gamma(t) \right), \tag{23}$$

where $K_\varphi > 0$ is a design parameter and $\gamma_{\text{ref,to}}$ corresponds to the orientation of the ground station's rails in the inertial reference frame. The rationale behind equation (23) is the following: from (13) we can write

$$\varphi(t) = \varphi_{\text{ref}}(t) - e_\varphi(t), \tag{24}$$

where the tracking error $e_\varphi(t)$ can be considered to be small thanks to the low-level controller of the roll dynamics (14). We further assume that

$$\dot{\psi}(t) \simeq \dot{\gamma}(t), \tag{25}$$

i.e. that the yaw rate and the rate of the course angle are similar, which is a reasonable assumption when the sideslip angle of the aircraft is small like in our application. Then, using (8) and (23)-(25), we have:

$$\dot{\gamma}(t) \simeq K_\varphi \left(\gamma_{\text{to}} - \gamma(t) \right), \tag{26}$$

which is (since $K_\varphi > 0$) a stable first-order system with time constant $\tau_\gamma = 1/K_\varphi$. Thus, under the proportional control law (23), the roll angle of the aircraft is controlled in order to track the desired course angle. Finally, we limit the turning radius of the aircraft to a minimum value $R_{\min}$ by setting the following bounds on the reference yaw rate (see equation (9)):

$$-\frac{|\dot{\boldsymbol{p}}(t)|^2}{g\, R_{\min}} \leq \varphi_{\text{ref}}(t) \leq \frac{|\dot{\boldsymbol{p}}(t)|^2}{g\, R_{\min}}. \tag{27}$$

Transition phase and figure-of-eight patterns. When the "safe-altitude" condition:

$$p_Z(t) \geq \underline{Z} \tag{28}$$

has been reached, the transition phase begins. The goal is to steer the aircraft back towards the ground station and engage a repetitive figure-of-eight pattern roughly above it, while at the same time continuing to ascend to the target altitude $Z_{\text{ref}} > \underline{Z}$. To achieve this result, in the airspeed controller we set a constant reference airspeed $v_{a,\text{ref}}(t) = v_{a,\text{ref,flight}}$ equal to the cruise speed of the aircraft. As regards the turning controller, we employ the same control law (23), but with a time-varying reference course angle $\gamma_{\text{ref}}(t)$, instead of the constant value $\gamma_{\text{ref,to}}$, in order to steer the aircraft towards two switching target points, which are fixed w.r.t. the ground and suitably chosen to achieve the desired flight patterns. In particular, let us consider two target points $\boldsymbol{p}^{\text{I}}$ and $\boldsymbol{p}^{\text{II}}$ defined in the inertial (X, Y, Z) plane. On the (X, Y) plane, these points are computed in order to be symmetrical w.r.t. to the location of the ground station along the take-off direction γ_{to}, and slightly shifted to one side along the direction perpendicular to γ_{to}. The altitude of the points is set equal to Z_{ref}. A graphical example of target points is shown in the experimental results of Fig. 5.

When condition (28) is detected, the target point farthest away from the aircraft is chosen as the active one, denoted as $\boldsymbol{p}^{\text{a}}$. Then, the reference course angle is computed as:

$$\gamma_{\text{ref}}(t) = \arctan\left(\frac{p_Y^{\text{a}}(t) - p_Y(t)}{p_X^{\text{a}}(t) - p_X(t)} \right), \tag{29}$$

i.e. the course angle corresponding to a straight line connecting the current (X, Y) position of the aircraft with that of the target. The switching of the active target point happens when the aircraft's (X, Y) position surpasses the position of the current target point, after projecting both positions on a direction corresponding to the take-off course $\gamma_{\text{ref,to}}$. As an example with $\gamma_{\text{ref,to}} = 0$, the corresponding switching rule would be:

$$\boldsymbol{p}^{\,\mathrm{a}}(t) = \begin{cases} \boldsymbol{p}^{\,\mathrm{I}} \text{ if } p_X(t) < -\dfrac{\Delta X_{\mathrm{ref}}}{2} + \delta_X \\ \boldsymbol{p}^{\,\mathrm{II}} \text{ if } p_X(t) > \dfrac{\Delta X_{\mathrm{ref}}}{2} - \delta_X \\ \boldsymbol{p}^{\,\mathrm{a}}(t^-) \text{ else} \end{cases} \tag{30}$$

where $\Delta X_{\mathrm{ref}} > 0$ is the chosen distance between target points along the take-off direction, $\delta_X > 0$ is a small tolerance (e.g. 0.5 m) to avoid possible numerical issues when computing the arctan function in (29), and $\boldsymbol{p}^{\,\mathrm{a}}(t^-)$ is the previous active target point, i.e. the target point at the previous sampling instant.

About the altitude controller, in this phase the aim is to regulate the aircraft Z position close to the reference Z_{ref}. To achieve this goal, we employ a static proportional feedback controller to compute $\theta_{\mathrm{ref}}(t)$:

$$\theta_{\mathrm{ref}}(t) = \frac{K_\theta}{|\dot{\boldsymbol{p}}(t)|}\left(Z_{\mathrm{ref}} - p_Z(t)\right) \tag{31}$$

where $K_\theta > 0$ is a design parameter. Similarly to what shown in (26) for the turning dynamics, from (16) we have:

$$\theta(t) = \theta_{\mathrm{ref}}(t) - e_\theta(t),$$

with small tracking error $e_\theta(t)$ thanks to the low-level controller. Then, considering also (11) and (31) we obtain:

$$\dot{p}_Z(t) \simeq K_\theta\left(Z_{\mathrm{ref}} - p_Z(t)\right), \tag{32}$$

which is a stable first-order system with time constant $\tau_\theta = 1/K_\theta$.

As a final remark before proceeding to the experimental results, aspects related to control input saturation, controller tuning, and closed-loop stability/robustness are not included in this paper for the sake of space, however they can be found in Fagiano et al. (2016a).

4. EXPERIMENTAL RESULTS

We implemented the ground station and aircraft controllers on a Speedgoat® real-time machine and on an Arduino MEGA 2560 board, respectively, see Fagiano et al. (2016c) and Fagiano et al. (2016a) for details. The parameters of the ground station controller are reported in Table 1, while the aircraft model parameters are shown in Table 2, together with the employed values of the onboard controller's parameters. The aircraft controller was implemented with a sampling frequency of 50 Hz.

Table 1. Ground station control parameters used for the experiments

T_s	0.001	s	x_{s}^{II}	0.1	m
$K_{\theta,\mathrm{s}}$	14	$\mathrm{N\,m\,rad^{-1}}$	$x_{\mathrm{s}}^{I,c}$	0.025	m
$K_{\dot{\theta},\mathrm{s}}$	2.5	$\mathrm{N\,m\,s\,rad^{-1}}$	$x_{\mathrm{s}}^{II,c}$	0.2	m
$K_{\dot{\theta},\mathrm{w}}$	1	$\mathrm{N\,m\,s\,rad^{-1}}$	$\underline{\dot{\theta}}_{\mathrm{ref,w}}^{\mathrm{fbck}}$	−10	$\mathrm{rad\,s^{-1}}$
$\overline{T}_{\mathrm{s}}$	26	Nm	$\overline{\dot{\theta}}_{\mathrm{ref,w}}^{\mathrm{fbck}}$	120	$\mathrm{rad\,s^{-1}}$
$\overline{T}_{\mathrm{w}}$	13	Nm	$\ddot{\theta}_{\mathrm{ref,w}}^{\mathrm{a}}$	−100	$\mathrm{rad\,s^{-2}}$
γ	1.2	-	$\ddot{\theta}_{\mathrm{ref,w}}^{\mathrm{c}}$	30	$\mathrm{rad\,s^{-2}}$
x_{s}^{I}	0.05	m	L	3.7	m

Table 2. Aircraft system and controller parameters for the experimental tests

System parameters		
a_φ	−2.3	$\mathrm{s^{-1}}$
b_φ	12.6	$\mathrm{s^{-2}}$
a_θ	−4.65	$\mathrm{s^{-1}}$
b_θ	30	$\mathrm{s^{-2}}$
C_D	0.05	-
ρ	1.2	$\mathrm{kg\,m^{-3}}$
A	0.3	$\mathrm{m^2}$
Controller parameters - inner loop		
$\lambda_{\varphi,1}$	−2.7	$\mathrm{s^{-1}}$
$\lambda_{\varphi,2}$	−3.1	$\mathrm{s^{-1}}$
$\lambda_{\theta,1}$	−2.7	$\mathrm{s^{-1}}$
$\lambda_{\theta,2}$	−3.1	$\mathrm{s^{-1}}$
K_{m}	0.5	$\mathrm{kg\,m^{-1}}$
$[\underline{u}_\varphi\ \overline{u}_\varphi]$	[−0.34 0.34]	rad
$[\underline{u}_\theta\ \overline{u}_\theta]$	[−0.34 0.34]	rad
$[\underline{u}_{\mathrm{m}}\ \overline{u}_{\mathrm{m}}]$	[0 20]	N
Controller parameters - outer loop		
K_φ	1	$\mathrm{s^{-1}}$
K_θ	0.1	$\mathrm{s^{-1}}$
$\underline{\ddot{p}}_{x,\mathrm{to}}$	20	$\mathrm{m\,s^{-1}}$
$v_{a,\mathrm{ref,to}}$	16	$\mathrm{m\,s^{-1}}$
$\theta_{\mathrm{ref,to}}$	0.69	rad
$\underline{Z}$	20	m
$\underline{R}_{\mathrm{min}}$	20	m
$v_{a,\mathrm{ref,flight}}$	13	$\mathrm{m\,s^{-1}}$
$[p_X^{\mathrm{I}}\ p_Y^{\mathrm{I}}\ p_Z^{\mathrm{I}}]$	[30 55 50]	m
$[p_X^{\mathrm{II}}\ p_Y^{\mathrm{II}}\ p_Z^{\mathrm{II}}]$	[−30 40 50]	m

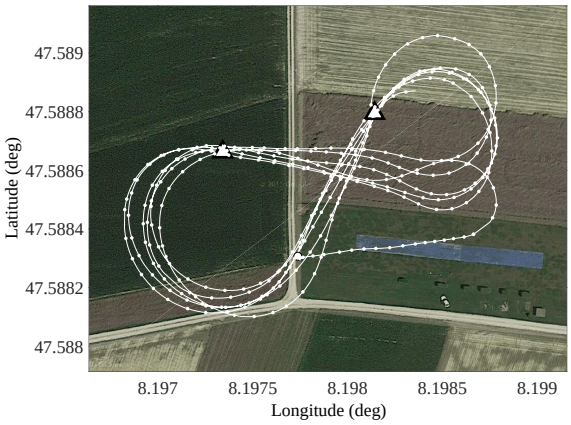

Fig. 5. Experimental results of a test with little wind at ground level. Flight pattern in GPS North-East coordinates, overlaid to a satellite map of the area. The target points $\boldsymbol{p}^{\,\mathrm{I}}$ and $\boldsymbol{p}^{\,\mathrm{II}}$ are marked with '△'. The white dots along the trajectory are position measurements down-sampled at 2 Hz.

We carried out several outdoor tests of fully autonomous take-off and flight using our experimental setup and the described control system. During the tests, the wind conditions changed from little/zero wind to front wind of about 4-5 m/s, to side wind of about 3-4 m/s. Thus, we were able to test the system both in undisturbed conditions (i.e. either no wind or little front wind) and in presence of moderate wind disturbance coming from different directions. A movie is available online (Fagiano et al. (2016b)), showing an autonomous take-off and flight test with the initial take-off, the transition phase and finally the figure-of-eight flights.

Due to space limitations we show here relatively few results and refer the reader to Fagiano et al. (2016a) for the results of repeated tests and more comments, and to Fagiano et al. (2016c) for more details specifically on the behavior of the ground station controller.

The flight trajectory projected on the inertial North-East plane is shown in Fig. 5, overlayed on a satellite image of the test area. The initial take-off phase on a straight line is clearly visible, as well as the transition to the figure-

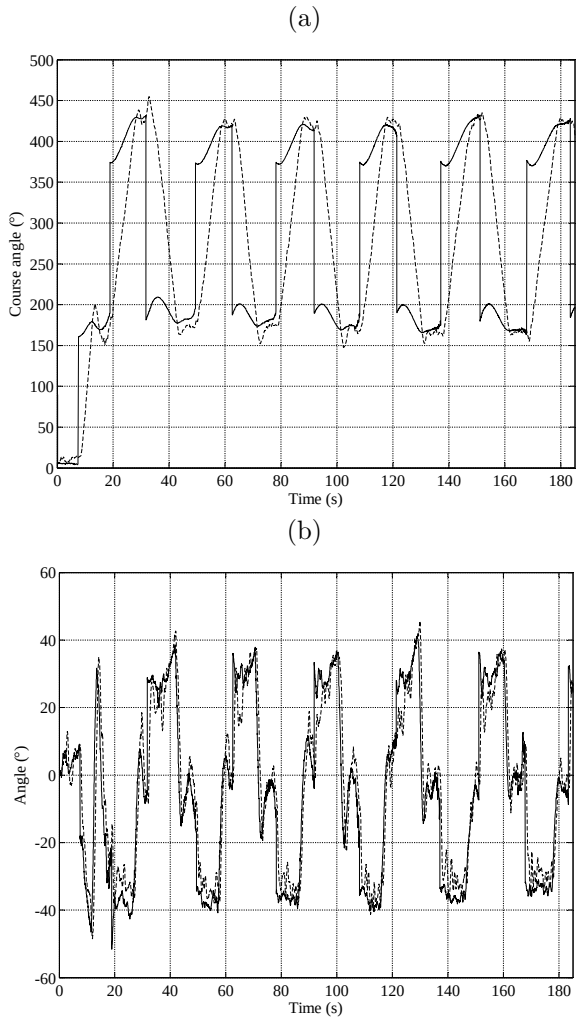

Fig. 6. Experimental results corresponding to Fig. 5, turning dynamics. (a) Course angle γ (dashed) and its reference $\gamma_{\rm ref}$ (solid) during tethered launch, climb and flight. (b) Roll angle φ (dashed) and its reference $\varphi_{\rm ref}$ (solid) in the same test.

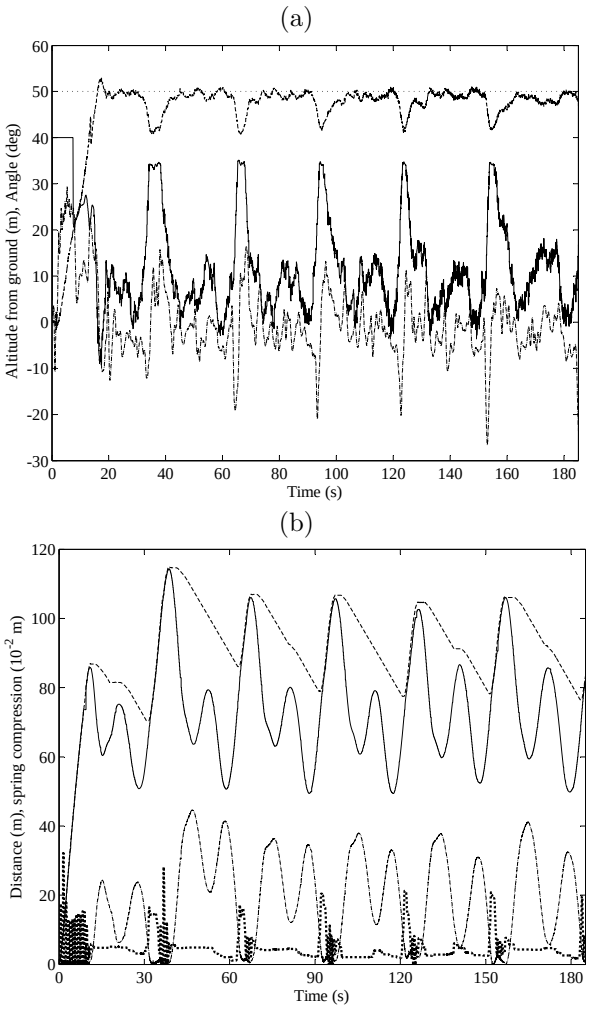

Fig. 7. Experimental results corresponding to Fig. 5, pitch and altitude dynamics. (a) Courses of the reference altitude $p_{Z,\rm ref}$ (dotted line), actual altitude p_Z (dashed), reference pitch $\theta_{\rm ref}$ (solid), and actual pitch θ (dash-dot). (b) Courses of the aircraft's distance from the ground station, $\|\boldsymbol{p}\|_2$ (solid line), of the tether length (dashed), of the spring compression (dotted) and of the slack tether length (dash-dotted). In plot (b), all plotted variables are in m, except for the spring compression in 10^{-2} m.

of-eight paths. To have an idea of the pattern size, the whole figure-of-eight is contained in a rectangle with sides of about 150m and 50m.

Figs. 6(a)-(b) show the behavior of the turning dynamics (roll and course angle controllers) during the test. The discontinuities in $\gamma_{\rm ref}(t)$ (Fig. 6(a), solid line) correspond to the switching instants between the target points. It can be clearly seen that the actual course angle $\gamma(t)$ (Fig. 6(a), dashed line) changes at a constant rate during these transitions, which corresponds to the turning rate at cruise speed and with the minimum turning radius of 20 m set in the controller. The corresponding roll angle $\varphi(t)$ (Fig. 6(b)) is approximately constant and equal to about 35° during these turns.

The closed-loop pitch and altitude motions are shown in Fig 7(a). The aircraft altitude quickly approaches the target of 50 m during the initial take-off and transition. The vertical rate is constant because, similarly to what happens for the rate of the course angle, the aircraft sets to constant pitch and airspeed, which according to our model (11) yields a constant vertical position rate. During flight, the high-level controller is able to track with good accuracy (about 3-4 m of error) the target altitude, see Fig. 7(a) e.g. between 45 s and 60 s, except for periodic, quick drops in the altitude which are limited to less than 10 m of tracking error. A comparison between the distance of the aircraft from the ground station and the tether length, shown in Fig. 7(b), reveals that such disturbances are due to the tether pull: during each figure-of-eight pattern the aircraft pulls on the tether for a fraction of the time and some length of slack line (also shown in Fig. 7(b)) is created. After the initial transient, the behavior of such a slack line becomes periodic as well, since the overall system (aircraft and ground station) converges to a stable periodic motion. The compression of the spring installed on the ground station is depicted in 7(b): we recall that this signal is used by the winch controller to regulate the winch reeling speed and decide whether to reel-out or reel-in, as described in Section 3.1.

As regards the propeller controller, Fig. 8 shows the courses of the reference airspeed and of the actual one, as well as the corresponding propeller thrust $u_{\rm m}$. Similarly

to the pitch controller, with no tether perturbations a small tracking error of about 0.5 $\mathrm{m\,s^{-1}}$ is achieved, while when the tether pulls on the aircraft a drop of airspeed is noticed, to which the controller reacts with an increase of thrust up to the maximum value. The loss of airspeed has consequences on all the other motions (pitch and roll), since it changes suddenly the angle of attack and the incoming flow speed. However, as already commented, the proposed controller is able to effectively cope with all such nonlinear effects.

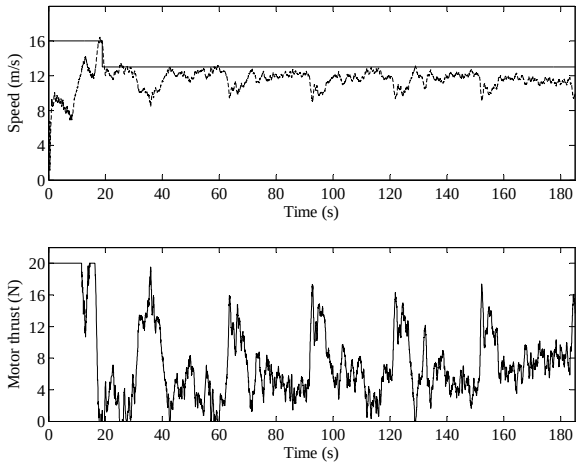

Fig. 8. Experimental results corresponding to Fig. 5, airspeed and motor thrust. Upper plot: courses of the reference airspeed $v_{a,\mathrm{ref}}$ (solid) and of the actual one, $v_a(t)$ (dashed). Lower plot: propeller thrust u_{m}.

5. CONCLUSIONS

We presented a control design approach for a system composed of a ground station, equipped with a controlled winch and a linear motion system, and a tethered aircraft. The control approach is distributed, without any exchange of information between the on-ground and onboard controllers. Coordination is achieved by means of a mass-spring system, installed on the ground station, whose compression is exploited by the winch controller to regulate the reeling speed. The presented approach includes both modeling and control design aspects and has been extensively tested in experiments, whose results have been reported here as well. The tests proved that take-off can be achieved in just 1.5 m with the considered aircraft. This is consistent with the theoretical results of Fagiano and Schnez (2015), where it is shown that, with a small additional power installed on-ground, the take-off for a power-generating system can be achieved in just about 10 m, irrespective of the aircraft's size, hence suggesting that this take-off approach can be technically and economically viable.

ACKNOWLEDGEMENTS

The authors would like to thank Alessandro Lauriola and Stefan Schmidt for their helpful contributions during the project.

REFERENCES

Ahrens, U., Diehl, M., and Schmehl, R. (eds.) (2013). *Airborne Wind Energy*. Springer, Berlin Heidelberg. doi:10.1007/978-3-642-39965-7.

Bontekoe, E. (2010). *Up! - How to Launch and Retrieve a Tethered Aircraft*. Master's thesis, TU Delft. Accessed in August 2015 at http://repository.tudelft.nl/.

Bormann, A., Ranneberg, M., Kövesdi, P., Gebhardt, C., and Skutnik, S. (2013). Development of a three-line ground-actuated airborne wind energy converter. In *Airborne Wind Energy*, chapter 24, 427–437. Springer, Berlin Heidelberg. doi:10.1007/978-3-642-39965-7_24.

Breukels, J., Schmehl, R., and Ockels, W. (2014). *Airborne Wind Energy*, chapter 16. Aeroelastic Simulation of Flexible Membrane Wings based on Multibody System Dynamics, 287. Green Energy and Technology. Springer-Verlag, Berlin.

Erhard, M. and Strauch, H. (2012). Control of towing kites for seagoing vessels. *IEEE Transactions on Control Systems Technology*, 21(5), 1629–1640. doi:10.1109/TCST.2012.2221093.

Erhard, M. and Strauch, H. (2015). Flight control of tethered kites in autonomous pumping cycles for airborne wind energy. *Control Engineering Practice*, 40, 13–26.

Fagiano, L. and Schnez, S. (2015). On the take-off of airborne wind energy systems based on rigid wings. *ArXiv e-prints: 1510.06701v1*, http://arxiv.org/abs/1510.06701v1.

Fagiano, L., Zgraggen, A.U., Morari, M., and Khammash, M. (2014). Automatic crosswind flight of tethered wings for airborne wind energy: modeling, control design and experimental results. *IEEE Transactions on Control System Technology*, 22(4), 1433–1447.

Fagiano, L., Nguyen-Van, E., Rager, F., Schnez, S., and Ohler, C. (2016a). Autonomous take off and flight of a tethered aircraft for airborne wind energy. *ArXiv e-prints: 1608.01889*, http://arxiv.org/abs/1608.01889.

Fagiano, L., Nguyen-Van, E., Rager, F., Schnez, S., and Ohler, C. (2016b). Autonomous tethered take-off and flight for airborne wind energy - movie. YouTube: https://www.youtube.com/watch?v=UPiTiHPXciE.

Fagiano, L., Nguyen-Van, E., Rager, F., Schnez, S., and Ohler, C. (2016c). A small-scale prototype to study the take-off of tethered rigid aircrafts for airborne wind energy. *ArXiv e-prints: 1608.01846*, http://arxiv.org/abs/1608.01846.

Goodwin, G.C., Graebe, S.F., and Salgado, M.E. (2001). *Control System Design*. Prentice-Hall, Upper Saddle River, NJ.

Gros, S., Zanon, M., and Diehl, M. (2013). Control of airborne wind energy systems based on nonlinear model predictive control & moving horizon estimation. In *European Control Conference (ECC) 2013*, 1017–1022. Zuerich, Switzerland, July 2013.

Loyd, M.L. (1980). Crosswind kite power. *Journal of Energy*, 4(3), 106–111. doi:10.2514/3.48021.

Ruiterkamp, R. and Sieberling, S. (2013). Description and preliminary test results of a six degrees of freedom rigid wing pumping system. In U. Ahrens, M. Diehl, and R. Schmehl (eds.), *Airborne Wind Energy*, chapter 26, 443–458. Springer, Berlin Heidelberg. doi:10.1007/978-3-642-39965-7_26.

van der Vlugt, R., Peschel, J., and Schmehl, R. (2013). Design and experimental characterization of a pumping kite power system. In U. Ahrens, M. Diehl, and R. Schmehl (eds.), *Airborne Wind Energy*, chapter 23, 403–425. Springer, Berlin Heidelberg. doi:10.1007/978-3-642-39965-7_23.

Zgraggen, A., Fagiano, L., and Morari, M. (2016). Automatic retraction and full-cycle operation for a class of airborne wind energy generators. *IEEE Transactions on Control Systems Technology*, 24(2), 594–698.